Article published in: Radio Science, vol. 50, pp.642-655, July 2015

Highly efficient full-wave electromagnetic analysis of 3D arbitrarily-shaped waveguide microwave devices using an integral equation technique

A . Vidal,[1] A. A. San-Blas,[2] F. D. Quesada-Pereira,[3] J. Pérez-Soler,[4] J. Gil,[4]

C. Vicente,[4] B. Gimeno[5], and V. E. Boria[1]

Corresponding author: A. A. San-Blas, Departamento de Ingeniería de Comunicaciones, Universidad Miguel Hernández de Elche, Avenida de la Universidad s/n, 03202 Elche (Alicante), Spain. (aasanblas@umh.es)

[1]Departamento de Comunicaciones - iTEAM, Universidad Politécnica de Valencia, Valencia, Spain.

[2]Departamento de Ingeniería de Comunicaciones, Universidad Miguel Hernández de Elche, Elche, Spain.

[3]Departamento de Tecnologías de la Información y las Comunicaciones, Universidad Politécnica de Cartagena, Cartagena, Spain.

[4]Aurora Software and Testing S.L., Valencia, Spain.

[5]Departamento de Física Aplicada y Electromagnetismo - ICMUV, Universidad de Valencia, Valencia, Spain.

A novel technique for the full-wave analysis of 3D complex waveguide devices is presented. This new formulation, based on the Boundary Integral-Resonant Mode Expansion (BI-RME) method, allows the rigorous full-wave electromagnetic characterization of 3D arbitrarily-shaped metallic structures making use of extremely low CPU resources (both time and memory). The unknown electric current density on the surface of the metallic elements is represented by means of Rao-Wilton-Glisson basis functions, and an algebraic procedure based on a singular value decomposition is applied to transform such functions into the classical solenoidal and non-solenoidal basis functions needed by the original BI-RME technique. The developed tool also provides an accurate computation of the electromagnetic fields at an arbitrary observation point of the considered device, so it can be used for predicting high-power breakdown phenomena. In order to validate the accuracy and efficiency of this novel approach, several new designs of band-pass waveguides filters are presented. The obtained results (S-parameters and electromagnetic fields) are successfully compared both to experimental data, and to numerical simulations provided by a commercial software based on the finite-element technique. The results obtained show that the new technique is specially suitable for the efficient full-wave analysis of complex waveguide devices considering an integrated coaxial excitation, where the coaxial probes may be in contact with the metallic insets of the component.

1. Introduction

Coaxial waveguides have been extensively used as coupling or feeding elements, both for ground and space applications in the microwave and millimeter-wave range. A great variety of classical waveguide filters, such as evanescent-mode and in-line filters, are usually fed using a coaxial excitation due to its high power handling capacity [*Uher et al.*, 1993]. Although a significant number of technical contributions have studied the electromagnetic characterization of coaxial fed rectangular waveguide devices over the last recent years, most of such investigations are not able to cope with the full-wave analysis of passive waveguide filters with an integrated coaxial excitation considering generalized coaxial probes (see, for instance, the magnetic feed used in [*Wang et al.*, 1998]).

Besides, in the case of more complex 3D waveguide components frequently used in critical receiver front-end applications, such as interdigital and comb-line waveguide filters, the coaxial probes are usually connected to the partial-height metallic posts of the input and output resonators with the aim of increasing the obtained coupling levels [*Yao et al.*, 1995]. To the authors' knowledge, few works have been devoted to the rigorous full-wave analysis (including the accurate computation of the related EM fields) of such configuration by means of modal techniques. Normally, the existing solvers make use of hybrid techniques, or are limited to coaxial probes with canonical geometries and to classical feed designs. For instance, a full-wave computer-aided design (CAD) tool for analyzing a collinear coaxial transition in rectangular waveguide is presented in [*Gerini and Guglielmi*, 2001]. Although the investigated structure considers a connection between a cylindrical coaxial probe and an inner metallic post, the shape of such post is restricted to a rectangular geometry. The same limitations are found in the work performed in [*Ruiz-Cruz et al.*, 2005], where a CAD tool for the analysis and design of rectangular waveguide filters with elliptic response was presented using the mode-matching method. Another remarkable contribution can be found in [*El Sabbagh et al.*, 2001], where a full-wave analysis of comb-line waveguide filters was performed. Although the authors claimed that a rigorous full-wave method was used in the analysis stage, the connection between the coaxial probes and the considered cylindrical posts was not taken into account in the multimodal analysis. More recently, complex waveguide filters were analyzed following a multimodal approach in [*Mira et al.*, 2013] and a very efficient CAD tool was presented. However, the proposed technique is not able to model the connection between the coaxial line and the considered cylindrical posts.

In order to overcome the cited drawbacks of the aforementioned contributions, the objective of this work is to present a novel technique for the efficient and rigorous full-wave analysis of complex waveguide devices considering an integrated coaxial excitation. The developed CAD tool, not only enables to cope with the electromagnetic characterization of generalized coaxial probes that may be in contact with the metallic elements present in the filter resonators, but it also provides a precise computation of the electromagnetic fields at an arbitrary observation point of the considered device. Therefore, this work constitutes a significant extension of the preliminary contribution presented by the authors in [*Quesada et al.*, 2010].

The full-wave analysis of the considered waveguide components is based on an extended formulation of the classical 3D Boundary Integral-Resonant Mode Expansion (BI-RME) method [*Arcioni et al.*, 2002]. The developed technique, which is very efficient from a computational point of view, combines the use of Rao-Wilton-Glisson (RWG) basis functions to represent the unknown electric current on the surface of the metallic elements of the analyzed component [*Rao et al.*, 1982], and the employment of an algebraic procedure based on a singular value decomposition (SVD) to cast such basis functions into the classical solenoidal and non-solenoidal basis functions needed by the original BI-RME technique [*Golub and Van Loan*, 1996].

It is very important to insist on the fact that previous contributions devoted to the analysis of waveguide components using the 3D BI-RME method cannot deal with the connection of the coaxial probe to the loading posts or to the resonator metallic walls. For instance, the set of the specialized basis functions used in [*Mira et al.*, 2013, 2005] does not permit to represent the connection between the coaxial line and the partial-height posts, since such functions are restricted to mesh only cylindrical geometries. A similar problem can be found when star-loop basis functions are used, that can not properly represent the contribution of the requested solenoidal basis functions (in particular if an open mesh needs to be employed, and the mesh is in contact with the cavity walls). In this case, the implementation of the SVD algorithm becomes crucial in order to correctly obtain the solenoidal and non-solenoidal contributions of the RWG basis functions.

The authors would like to stress the fact that the implemented software could be also employed for analyzing other 3D complex waveguide structures in which the coaxial excitation may not be present, and a general surface meshing is required. This is the case, for instance, of inductive iris waveguide filters with rounded corners in the longitudinal section of the component, which are frequently used in waveguide diplexers. Note that the full-wave analysis of such complex structures cannot be addressed using classical approaches, as the full-wave method used in [*Cogollos et al.*, 2001].

Next, the theory related to the extension of the 3D BI-RME method using RWG basis functions is presented, and the SVD algorithm is applied to yield the solenoidal and non-solenoidal contributions of the electric current density. Detailed expressions of the electric and the magnetic fields inside the cavity are provided, as well. Afterwards, several designs of complex waveguide components are presented in order to validate the accuracy of the proposed technique. In addition, the electromagnetic fields inside the designed components have been calculated using the developed tool, and they have been successfully compared to the simulated data provided by a commercial software based on the finite-element technique.

2. Full-wave analysis of complex waveguide filters using advanced modal techniques

The main objective of this section is to present a full-wave analysis procedure for the efficient characterization of complex waveguide filters including an integrated coaxial excitation. The developed technique, which is based on the 3D Boundary Integral-

Resonant Mode Expansion method [*Arcioni et al.*, 2002; *Mira et al.*, 2005], allows the connection between the coaxial probe used to excite the component and any metallic element placed inside the filter resonator. To this aim, the classical 3D BI-RME technique, which was originally formulated in terms of solenoidal and non-solenoidal basis functions employed to represent the unknown electric current density, has been properly extended to cope with the use of the more general Rao-Wilton-Glisson basis functions [*Rao et al.*, 1982].

This novel extension allows us to mesh, without any geometrical restriction, the surface of the metallic insets of the filter using triangular cells, thus obtaining a very flexible tool for the analysis and design of advanced 3D waveguide filters that may be fed (or not) by generalized coaxial probes. Besides, the analytical expressions of the electric and the magnetic fields at an arbitrary observation point of the considered device are also derived and discussed, thus finally providing a rigorous tool that can be employed, as well, for evaluating breakdown phenomena, such as the well-known multipactor and corona effects [*Cameron et al.*, 2007].

In order to obtain the generalized admittance matrix (GAM) of lossless microwave devices with an arbitrary 3D geometry, the classical formulation of the BI-RME method yields a matrix problem in the following form [*Mira et al.*, 2005]:

$$(\mathbf{A} - k^2\mathbf{B})\mathbf{x} = \mathbf{C}\mathbf{v} \tag{1}$$

where k is the wavenumber, $\mathbf{v}$ represents the excitation of the structure, and $\mathbf{x}$ constitutes the unknown of the problem, which is related to the electric current density on the surface of the metallic elements (see more details in [*Mira et al.*, 2005]). Moreover, when a set of RWG basis functions is used to model the unknown electric current density on the metallic inset surfaces of the structure, the classical expressions of the BI-RME matrices $\mathbf{A}$, $\mathbf{B}$ and $\mathbf{C}$ used in (1) must be properly updated as follows:

$$\mathbf{A}^{\mathbf{RWG}} = \begin{bmatrix} \mathbf{K}^4 & \mathbf{0} \\ \mathbf{0} & \mathbf{S}^{\mathbf{RWG}} \end{bmatrix} \tag{2a}$$

$$\mathbf{B}^{\mathbf{RWG}} = \begin{bmatrix} \mathbf{K}^2 & \mathbf{R}^{\mathbf{RWG}} \\ (\mathbf{R}^{\mathbf{RWG}})^T & \mathbf{V}^{\mathbf{RWG}} \end{bmatrix} \tag{2b}$$

$$\mathbf{C}^{\mathbf{RWG}} = \begin{bmatrix} -\mathbf{KF} \\ -\mathbf{L}^{\mathbf{RWG}} \end{bmatrix} \tag{2c}$$

In the previous expressions, $\mathbf{K}$ is a diagonal matrix containing the first M resonant wavenumbers k_m of a canonical rectangular cavity, while the rest of matrices can be defined as:

$$\mathbf{S}^{\mathbf{RWG}}{}_{rp} = \int_S \int_{S'} \nabla_S \cdot \mathbf{f}_r(\mathbf{r}) g^e(\mathbf{r}, \mathbf{r}') \nabla'_S \cdot \mathbf{f}_p(\mathbf{r}')\, dS\, dS' \tag{3a}$$

$$\mathbf{V}^{\mathbf{RWG}}{}_{rp} = \int_S \int_{S'} \mathbf{f}_r(\mathbf{r}) \cdot \overline{\mathbf{G}}_{\mathbf{0}}^{\mathbf{A}}(\mathbf{r}, \mathbf{r}') \cdot \mathbf{f}_p(\mathbf{r}')\, dS\, dS' \tag{3b}$$

$$\mathbf{R}^{\mathbf{RWG}}{}_{mp} = \int_S \mathbf{E}_m(\mathbf{r}) \cdot \mathbf{f}_p(\mathbf{r})\, dS \tag{3c}$$

$$\mathbf{L}^{\mathbf{RWG}}{}_{rn} = \int_S \int_{S'} \mathbf{f}_r(\mathbf{r}) \cdot \nabla_S \times \overline{\mathbf{G}}_{\mathbf{0}}^{\mathbf{F}}(\mathbf{r}, \mathbf{r}') \cdot \mathbf{h}_n(\mathbf{r}')\, dS\, dS' - \frac{1}{2} \int_S \mathbf{f}_r(\mathbf{r}') \cdot \mathbf{e}_n(\mathbf{r})\, dS \tag{3d}$$

$$\mathbf{F}_{mn} = \int_S \mathbf{H}_m(\mathbf{r}) \cdot \mathbf{h}_n(\mathbf{r})\, dS \tag{3e}$$

where $\mathbf{f}_r(\mathbf{r})$ denotes a vector with the RWG basis functions; $\mathbf{E}_m(\mathbf{r})$ and $\mathbf{H}_m(\mathbf{r})$ are, respectively, the m-th electric and magnetic-type resonant modes of the considered rectangular resonator; $g^e(\mathbf{r}, \mathbf{r}')$ represents the electric-type scalar Green's function related to a rectangular cavity; $\overline{\mathbf{G}}_{\mathbf{0}}^{\mathbf{A}}(\mathbf{r}, \mathbf{r}')$ and $\overline{\mathbf{G}}_{\mathbf{0}}^{\mathbf{F}}(\mathbf{r}, \mathbf{r}')$ are, respectively, the electric and magnetic-type quasi-static dyadic Green's functions of the boxed resonator; and $\mathbf{e}_n(\mathbf{r})$ and $\mathbf{h}_n(\mathbf{r})$ represent the n-th electric and magnetic vector mode functions of the waveguide access ports.

Once the elements of the matrices deduced in (3) have been computed, we need to transform them into the matrices used in the classical BI-RME formulation, which are referred to a solenoidal and non-solenoidal set of basis functions [*Mira et al.*, 2005]. To this aim, a singular value decomposition (SVD) algorithm performed on matrix $\mathbf{S^{RWG}}$ is proposed, in order to generate the aforementioned transformation matrices [*Golub and Van Loan*, 1996]. Note that the application of an SVD approach is needed in order to yield a proper projection of the RWG basis functions onto their non-solenoidal (column-space) and solenoidal (null-space) counterparts needed in the classical formulation. Therefore, the SVD decomposition of matrix $\mathbf{S^{RWG}}$ yields:

$$\mathbf{S^{RWG}} = \mathbf{U\Lambda V} \tag{4}$$

In this expression, $\mathbf{U}$ is an orthogonal matrix whose columns are the eigenvectors of $\mathbf{S^{RWG}}(\mathbf{S^{RWG}})^T$, and $\mathbf{V}^T$ is an orthogonal matrix containing the eigenvectors of $(\mathbf{S^{RWG}})^T\mathbf{S^{RWG}}$. Besides, $\mathbf{\Lambda}$ is a diagonal matrix with the singular values of matrix $\mathbf{S^{RWG}}$. The non-zero singular values are arranged in increasing order and they correspond to the absolute value of the eigenvalues of matrix $\mathbf{S^{RWG}}$ (note that this matrix is symmetrical). The N_{nsol} non-zero singular values are related to the non-solenoidal basis functions, while the N_{sol} null singular values are associated with the solenoidal basis functions of the classical BI-RME formulation. Therefore, the total number of RWG basis functions is equal to $N_{tot} = N_{sol} + N_{nsol}$.

The SVD decomposition of the matrix $\mathbf{S}^{\mathbf{RWG}}$ provides the transformation matrices $\mathbf{t}_V$ and $\mathbf{t}_W$ as follows:

$$\mathbf{t}_V = \mathbf{U}(:, 1 : N_{nsol})^T \tag{5a}$$

$$\mathbf{t}_W = \mathbf{U}(:, N_{nsol} + 1 : N_{tot})^T \tag{5b}$$

Next, the solenoidal $\mathbf{W}$ and non-solenoidal $\mathbf{V}$ basis functions can be readily obtained using the relations [*Conciauro et al.*, 2000]:

$$\begin{pmatrix} W_1 \\ W_2 \\ \vdots \\ W_{N_{sol}} \end{pmatrix} = \mathbf{t}_W \begin{pmatrix} f_1 \\ f_2 \\ \vdots \\ f_{N_{tot}} \end{pmatrix} \tag{6a}$$

$$\begin{pmatrix} V_1 \\ V_2 \\ \vdots \\ V_{N_{nsol}} \end{pmatrix} = \mathbf{t}_V \begin{pmatrix} f_1 \\ f_2 \\ \vdots \\ f_{N_{tot}} \end{pmatrix} \tag{6b}$$

Finally, the computation of matrix $\mathbf{U}$ allows us to derive the set of the classical BI-RME matrices (see [*Mira et al.*, 2005]) needed to obtain the generalized admittance matrix of the analyzed component:

$$\mathbf{S} = \mathbf{t}_V \mathbf{S}^{\mathbf{RWG}} \mathbf{t}_V^T \tag{7a}$$

$$\mathbf{V} = \mathbf{t}_V \mathbf{V}^{\mathbf{RWG}} \mathbf{t}_V^T \tag{7b}$$

$$\mathbf{W} = \mathbf{t}_W \mathbf{V}^{\mathbf{RWG}} \mathbf{t}_W^T \tag{7c}$$

$$\mathbf{Q} = \mathbf{t}_V \mathbf{V}^{\mathbf{RWG}} \mathbf{t}_W^T \tag{7d}$$

$$\mathbf{R}' = \mathbf{R}^{\mathbf{RWG}} \mathbf{t}_V^T \tag{7e}$$

$$\mathbf{R}'' = \mathbf{R}^{\mathbf{RWG}} \mathbf{t}_W^T \tag{7f}$$

$$\mathbf{L}' = \mathbf{t}_V \mathbf{L}^{\mathbf{RWG}} \tag{7g}$$

$$\mathbf{L}'' = \mathbf{t}_W \mathbf{L}^{\mathbf{RWG}} \tag{7h}$$

Although the calculation of the previous matrices derived in (7) involves several matrix multiplications and matrix inversions, such computation can be accelerated using QR decompositions. In addition, it is important to point out that, on account of the SVD decomposition performed on matrix $\mathbf{S}^{\mathbf{RWG}}$, the new matrix $\mathbf{S}$ presents now a compact diagonal form thanks to the multiplication with its corresponding non-solenoidal transformation matrix, and the values of the diagonal are directly equal to the non-zero singular values of matrix $\mathbf{\Lambda}$. As a consequence, the generalized eigenvalue problem obtained starting from equation (1) and considering $\mathbf{v} = 0$, becomes a standard eigenvalue problem since the new matrix $\mathbf{A}$ is now diagonal. Note that such eigenvalue problem provides the resonant modes of the structure, and it has to be solved in order to obtain the GAM of the analyzed device in the form of pole expansions [*Mira et al.*, 2005].

2.1. Calculation of the electromagnetic fields in the structure

The electric current density on the surface of the metallic insets of the structure can be written as [*Conciauro et al.*, 2000]:

$$\mathbf{J}(\mathbf{r}) = \frac{-jk}{\eta}\mathbf{b}\,\mathbf{t}_V\,\mathbf{f}(\mathbf{r}) + \frac{1}{\eta}\mathbf{c}\,\mathbf{t}_W\,\mathbf{f}(\mathbf{r}) \tag{8}$$

In the previous equation, $\mathbf{f}(\mathbf{r})$ denotes the RWG basis functions; $\mathbf{b}$ is a vector containing the expansion coefficients related to the non-solenoidal basis functions; and $\mathbf{c}$ represents an auxiliary vector defined by [*Mira et al.*, 2005]:

$$\mathbf{c} = \mathbf{W}^{-1}[(1/jk)\mathbf{L}''\,\mathbf{v} + jk(\mathbf{Q}^T\,\mathbf{b} + \mathbf{R}''^T\,\mathbf{a})] \tag{9}$$

where the matrices $\mathbf{W}$, $\mathbf{L}''$, $\mathbf{Q}$, and $\mathbf{R}''$ have been defined in (7); $\mathbf{v}$ is the excitation vector used in (1), and $\mathbf{a}$ is a vector containing the so-called mode amplitudes:

$$a_m = \frac{1}{k_m^2(k_m^2 - k^2)}\left(jk\eta\int_S \mathbf{E}_m(\mathbf{r})\cdot\mathbf{J}(\mathbf{r})\,dS - k_m\sum_{n=1}^{N} v_n\int_S \mathbf{H}_m(\mathbf{r})\cdot\mathbf{h}_n(\mathbf{r})\,dS\right) \tag{10}$$

being N the number of modes considered in the waveguide access ports. Moreover, note that vectors $\mathbf{a}$ and $\mathbf{b}$ are readily obtained after solving the matrix problem deduced in (1), since the state vector $\mathbf{x} = [\mathbf{a}\ \mathbf{b}]^T$ [*Mira et al.*, 2005].

Next, starting from (8), we previously define:

$$\mathbf{d} = \frac{-jk}{\eta}\mathbf{b}\,\mathbf{t}_V + \frac{1}{\eta}\mathbf{c}\,\mathbf{t}_W \tag{11}$$

Then, making use of the mode amplitudes defined in (10), the desired expressions for the electric and magnetic fields in the structure can be finally written in terms of both the coefficients $\mathbf{d}$ and the RWG basis functions used to represent the electric current density:

$$\begin{aligned}
\mathbf{E}(\mathbf{r}) = {} & \frac{\eta}{j\,k}\nabla \int_S g^e(\mathbf{r},\mathbf{r}')\,\nabla'_S \cdot \left(\sum_{n_b=1}^{N_{tot}} d_{n_b}\mathbf{f}_{n_b}(\mathbf{r}')\right) dS' + \frac{1}{2}\sum_{n=1}^{N} v_n \mathbf{e}_n(\mathbf{r}) \\
& - jk\eta \int_S \overline{\mathbf{G}}_{\mathbf{0}}^{\mathbf{A}}(\mathbf{r},\mathbf{r}') \cdot \sum_{n_b=1}^{N_{tot}} d_{n_b}\mathbf{f}_{n_b}(\mathbf{r}')\,dS' + k^2 \sum_{m=1}^{M} a_m \mathbf{E}_m(\mathbf{r}) \\
& + \sum_{n=1}^{N} v_n \int_S \nabla \times \overline{\mathbf{G}}_{\mathbf{0}}^{\mathbf{F}}(\mathbf{r},\mathbf{r}') \cdot \mathbf{h}_n(\mathbf{r}')\,dS' \qquad (12a)
\end{aligned}$$

$$\begin{aligned}
\mathbf{H}_T(\mathbf{r}) = {} & \frac{1}{2}\left(\sum_{n_b=1}^{N_{tot}} d_{n_b}\mathbf{f}_{n_b}(\mathbf{r})\right) \times \mathbf{n} - \frac{1}{jk\eta}\sum_{n=1}^{N} v_n \nabla_s \int_S g^m(\mathbf{r},\mathbf{r}')\nabla'_S \cdot \mathbf{h}_n(\mathbf{r}')\,dS' \\
& + \int_S \nabla \times \overline{\mathbf{G}}_{\mathbf{0}}^{\mathbf{A}}(\mathbf{r},\mathbf{r}') \cdot \sum_{n_b=1}^{N_{tot}} d_{n_b}\mathbf{f}_{n_b}(\mathbf{r}')\,dS' - \frac{jk}{\eta}\sum_{m=1}^{M} a_m k_m \mathbf{H}_m(\mathbf{r}) \\
& + \frac{jk}{\eta}\sum_{n=1}^{N} v_n \left(\int_S \overline{\mathbf{G}}_{\mathbf{0}}^{\mathbf{F}}(\mathbf{r},\mathbf{r}') \cdot \mathbf{h}_n(\mathbf{r}')\,dS' - \sum_{m=1}^{M} \frac{\mathbf{H}_m(\mathbf{r})}{k_m^2}\int_S \mathbf{H}_m(\mathbf{r}') \cdot \mathbf{h}_n(\mathbf{r}')\,dS'\right) \\
& \qquad (12b)
\end{aligned}$$

where $\mathbf{n}$ is the inward unit vector normal to the surface; and $g^m(\mathbf{r},\mathbf{r}')$ represents the magnetic-type scalar Green's function related to a rectangular resonator. Note that the previous expressions concerning the electric and magnetic fields contain some integrals involving the static scalar and dyadic Green's functions of a boxed resonator, and the RWG basis functions. Although such integrals can be evaluated numerically using specific integration rules intented for triangular regions [*Cools*, 1999], a drastical loss of accuracy is expected as the observation point approaches the source point, due to the well-known singular and hyper-singular behaviour of the Green's functions. In the appendix A, a solution to overcome such problem is addressed and discussed in detail, and some useful closed expressions are provided.

3. Numerical and experimental results

Next, we proceed to verify the accuracy and the computational efficiency of the implemented CAD tool. To this aim, the proposed technique is used to design three advanced waveguide components: an interdigital filter with an integrated collinear coaxial feed, an inductive iris waveguide filter with rounded corners in the longitudinal section of the component, and an evanescent-mode filter excited using a top coaxial feed (vertical configuration).

The first proposed design consists of a 5-resonator interdigital band-pass filter including a coaxial feed (collinear configuration) in which the probe is in contact with the metallic posts of the input and output resonators (see Fig. 2). The transverse dimensions of each rectangular resonator are $15.87\,\mathrm{mm} \times 50\,\mathrm{mm}$, and the radius of all the considered cylindrical posts and tuning screws is 3.0 mm. Regarding the coaxial lines, the external radius is 3.0 mm, the internal radius is 0.65 mm (air filled), the length of the probes (up to the center of the metallic post) is 9.0 mm, and the feed point is located at a height of 6.79 mm. The rest of dimensions can be found in Table 1 and Table 2.

In Fig. 3, we have represented the electrical response of the designed interdigital filter. Our simulated results are in excellent agreement with the numerical data provided by a commercial software tool based on the finite-element technique (Ansys HFSS), thus validating the accuracy of the proposed analysis method. In order to achieve the convergent results presented in Fig. 3, 20 accessible modes have been considered in the analysis stage (only 10 modes in the coaxial lines). For meshing purposes, 1400 RWG basis functions have been employed on each cavity resonator, and 1290 RWG basis functions have been used in the excitation cavities. Besides, the CPU time required for the computation of a complete frequency response (150 frequency points) was only 28.9 s (6-core processor), thus demonstrating the computational efficiency of the developed CAD tool (HFSS took about 5 min per frequency point).

Finally, the electric field inside the designed interdigital filter has been computed at $f = 1.75$ GHz (central frequency of the passband of the filter) on the $x = 0$ plane (in Fig. 2, the origin of coordinates lies in the center of the input coaxial waveguide port). The obtained results, which are successfully compared with the data provided by Ansys HFSS, have been represented in Fig. 4. Note that the computation of the electric field may be very useful for predicting high-power breakdown phenomena, such as the well-known corona and multipactor effects.

The next example, courtesy of Virginia Diodes Inc., deals with the design of an E-band inductive iris waveguide filter with rounded corners in the longitudinal section of the component, as represented in Fig. 5. The filter has been implemented in WR-10 rectangular waveguide ($a = 2.54$ mm, $b = 1.27$ mm), and the radius of the rounded corners is equal to 0.251 mm. The length of the inductive irises is 0.124 mm, and the corresponding widths can be found in Table 3. Moreover, the lengths of the waveguide resonators are listed in Table 4.

This inductive filter has been successfully manufactured and measured, and the obtained S-parameters have been depicted in Fig. 6. The results obtained with the developed CAD tool are successfully compared both to measurements from Virginia

Diodes Inc., and to the simulations obtained with Ansys HFSS. The analysis of this advanced component was performed using 10 accessible modes and 380 RWG basis functions, while the CPU effort was about 16 s over 500 frequency points (Ansys HFSS needed about 8 min per frequency point to achieve convergent results).

Finally, we have computed the magnetic field inside the considered inductive filter, concretely on the $y = 0$ plane (in Fig. 5, the origin of coordinates lies in the center of the input rectangular waveguide port). Note that the calculation of the magnetic field is very important to identify the zones of the filter with high levels of Joule effect losses (i.e. high temperature zones), and it is specially useful when handling high-power signals. Therefore, an accurate computation of the magnetic field allows the microwave designer to reach an optimum implementation of the proper baseplates to cool the component. In Fig. 7 we have depicted the computed magnetic field at $f = 83$ GHz, and a very good agreement is observed with regard to the data obtained using Ansys HFSS.

The last validation example addresses the design of an X-band evanescent-mode filter composed of the cascade connection of 7 rectangular cavities whose transverse dimensions are 9.0×10.15 mm. A top coaxial feed has been considered in this new design, as represented in Fig. 8 (note that the first and the last cavities contain the coaxial excitation). The internal and external radii of the coaxial lines are 0.635 mm and 2.11 mm, respectively, and the relative permittivity is 2.08. Besides, the height of the coaxial probes is 5.836 mm, the feed point is located at a distance of 3.0 mm, and the length of the cavities containing the coaxial lines is 6.0 mm. On the other hand, the radius of the considered cylindrical posts is 1.25 mm. The lengths of the rest of cavities of the filter (i.e. those loaded with the cylindrical posts), as well as the height of the considered resonant posts, are collected in Table 5. Moreover, the lengths of the uniform waveguide sections used between the rectangular cavities can be found in Table 6.

The electrical response of the designed evanescent-mode filter has been represented in Fig. 9, where an excellent agreement is again observed between authors' simulations and Ansys HFSS numerical data. In this design, 40 accessible modes have been employed in the rectangular waveguides, and 1025 RWG basis functions have been used for meshing each resonant cavity (the cavities containing the coaxial lines have required 500 RWG basis functions). The analysis of this filter only needed 38 s over 200 frequency points, while the simulation with Ansys HFSS took about 15 min per frequency point.

4. Conclusion

In this work, a novel CAD tool for the rigorous analysis and design of advanced waveguide components with an integrated coaxial excitation has been proposed. With respect to previous works on the same subject, the proposed technique is able to cope, for the first time to the authors' knowledge, with the full-wave electromagnetic characterization of generalized coaxial probes that can be in contact with the metallic insets of the considered device, without resorting to hybrid techniques. To this aim, the original 3D BI-RME method has been properly modified to allow the use of RWG basis functions for meshing purposes. An algebraic procedure based on a SVD decomposition has been also applied to cast such RWG basis functions into the classical solenoidal and non-solenoidal basis functions, thus allowing a rigorous representation of the unknown electric current density. Moreover, accurate closed expressions for the computation of the electromagnetic fields at an arbitrary observation point of the considered device have been derived. The proposed method has been fully validated through the presentation of several new designs concerning complex band-pass waveguide filters. The obtained electrical responses, as well as the electromagnetic fields inside the considered devices, have been successfully compared both to experimental and simulated data.

Appendix A: Computation of the singular terms related to the calculation of the electromagnetic field

In section 2.1, the following set of integrals was derived:

$$\mathbf{I}_{E_1}(\mathbf{r}) = \frac{\eta}{j\,k} \int_{S_n} \nabla g^e(\mathbf{r}, \mathbf{r}') \nabla' \cdot \mathbf{f}_n(\mathbf{r}') dS' \tag{A1a}$$

$$\mathbf{I}_{E_2}(\mathbf{r}) = jk\eta \int_{S_n} \overline{\mathbf{G}}_{\mathbf{0}}^{\mathbf{A}}(\mathbf{r}, \mathbf{r}') \cdot \mathbf{f}_n(\mathbf{r}')\, dS' \tag{A1b}$$

$$\mathbf{I}_{H_1}(\mathbf{r}) = \int_{S_n} \nabla \times \overline{\mathbf{G}}_{\mathbf{0}}^{\mathbf{A}}(\mathbf{r}, \mathbf{r}') \cdot \mathbf{f}_n(\mathbf{r}')\, dS' \tag{A1c}$$

where $\mathbf{r}$ and $\mathbf{r}'$ are, respectively, the so-called observation and source points, and $\mathbf{f}_n(\mathbf{r}')$ represents the n-th RWG basis functions. Note that the previous integrals become singular when the observation point is close to the source point. In order to cope with this situation, the integration of the singular terms requires a proper analytical treatment. The first step consists of decomposing the Green's functions into a singular and a regular term, with the aim of rewriting the set of integrals in (A1) as follows:

$$\mathbf{I}_{E_1}(\mathbf{r}) = \mathbf{I}_{E_1}^{(reg)}(\mathbf{r}) + \mathbf{I}_{E_1}^{(sing)}(\mathbf{r}) \tag{A2a}$$

$$\mathbf{I}_{E_2}(\mathbf{r}) = \mathbf{I}_{E_2}^{(reg)}(\mathbf{r}) + \mathbf{I}_{E_2}^{(sing)}(\mathbf{r}) \tag{A2b}$$

$$\mathbf{I}_{H_1}(\mathbf{r}) = \mathbf{I}_{H_1}^{(reg)}(\mathbf{r}) + \mathbf{I}_{H_1}^{(sing)}(\mathbf{r}) \tag{A2c}$$

On the one hand, the regular terms $\mathbf{I}^{(reg)}(\mathbf{r})$ can be integrated employing very few integration points since the singularity has been extracted. On the other hand, on account of the investigation performed in [*Bressan et Conciauro*, 1985] for obtaining the singular terms of the scalar and dyadic Green's function in the Coulomb gauge, the singular terms of the previous integrals can be expressed in the following form:

$$\mathbf{I}_{E_1}^{(sing)}(\mathbf{r}) = \frac{\eta}{4j\,k\pi} \int_{S'} \nabla \frac{1}{R} \nabla' \cdot \mathbf{f}_n(\mathbf{r}') dS' \tag{A3a}$$

$$\mathbf{I}_{E_2}^{(sing)}(\mathbf{r}) = \frac{jk\eta}{8\pi} \int_{S'} \frac{1}{R} \left(\bar{\mathbf{I}} + \frac{\mathbf{RR}}{R^2} \right) \cdot \mathbf{f}_n(\mathbf{r}')\, dS' \tag{A3b}$$

$$\mathbf{I}_{H_1}^{(sing)}(\mathbf{r}) = \frac{1}{8\pi} \int_{S'} \nabla \times \frac{1}{R} \left(\bar{\mathbf{I}} + \frac{\mathbf{RR}}{R^2} \right) \cdot \mathbf{f}_n(\mathbf{r}')\, dS' \tag{A3c}$$

where $\bar{\mathbf{I}}$ is the unit dyadic, $\mathbf{R} = \mathbf{r} - \mathbf{r}'$ and $R = |\mathbf{R}|$. Next, we demonstrate that the singular integrals derived in (A3) can be analytically treated to finally yield closed expressions that enable us to obtain very accurate results for the electromagnetic field near the source points.

A1. Calculation of $\mathbf{I}_{E_1}^{(sing)}(\mathbf{r})$

As the divergence of a RWG basis function is a constant value (see [*Rao et al.*, 1982]), the proper evaluation of this singular integral starts from the computation of the next expression:

$$\mathbf{I}_1(\mathbf{r}) = \nabla \int_{S'} \frac{1}{R}\, dS' = \nabla I_{aux,1} \tag{A4}$$

In virtue of the results obtained in [*Wilton et al.*, 1984], the integral (A4) can be expressed in terms of three line integrals. Let us consider the geometrical variables depicted in Fig. 1, where we have represented a triangular cell employed when a surface is meshed using classical RWG basis functions. In this figure, a line segment (i) of such triangular cell has been drawn using a bold line. Next, we define the following variables:

$$d_{(i)} = (\mathbf{r} - \mathbf{r}_{2\,(i)}) \cdot \hat{\mathbf{n}} = (\mathbf{r} - \mathbf{r}_{1\,(i)}) \cdot \hat{\mathbf{n}} \tag{A5a}$$

$$\mathbf{r}_{proy} = \mathbf{r} - d\hat{\mathbf{n}} \tag{A5b}$$

$$\mathbf{P}_{o\,(i)} = \left[(\mathbf{r}_{2\,(i)} - \mathbf{r}) \cdot \hat{\mathbf{u}}_{(i)}\right] \cdot \hat{\mathbf{u}}_{(i)} \tag{A5c}$$

$$P_{o\,(i)} = |\mathbf{P}_{o\,(i)}| \tag{A5d}$$

$$R_{o\,(i)} = \sqrt{d^2 + P_{o\,(i)}^2} \tag{A5e}$$

$$l_{1\,(i)} = (\mathbf{r}_{1\,(i)} - \mathbf{r}) \cdot \hat{\mathbf{l}}_{(i)} \tag{A5f}$$

$$l_{2\,(i)} = (\mathbf{r}_{2\,(i)} - \mathbf{r}) \cdot \hat{\mathbf{l}}_{(i)} \tag{A5g}$$

$$R_{1\,(i)} = |\mathbf{r} - \mathbf{r}_{1\,(i)}| \tag{A5h}$$

$$R_{2\,(i)} = |\mathbf{r} - \mathbf{r}_{2\,(i)}| \tag{A5i}$$

where $d_{(i)}$ is the distance between the observation point and the plane Π that contains the closed surface; $\hat{\mathbf{n}}$ represents a unit vector normal to the considered surface; $P_{o\,(i)}$ denotes the distance between the observation point projected onto the plane ($\mathbf{r}_{proy}$) and the line containing the line segment (i); and $\mathbf{P}_{o\,(i)}$ is a unit vector directed along such distance. Moreover, $\hat{\mathbf{u}}_{(i)}$ is an outward-pointing unit vector normal to the line segment (i), and $\hat{\mathbf{l}}_{(i)}$ is a unit vector directed along the line segment (i). Finally, the distances $R_{1\,(i)}$ and $R_{2\,(i)}$ are defined between the observation point and the two vertexes of the line segment (i); and $l_{1\,(i)}$ and $l_{2\,(i)}$ represent the coordinates of such vertexes expressed in terms of a parametric variable directed along the considered line segment, and considering the projection of the observation point onto the line containing the line segment (i) as the origin of this auxiliary reference system (see Fig. 1).

Now, the auxiliary integral $I_{aux,1}$ can be written as:

$$I_{aux,1} = \int_{S'} \frac{1}{R}\, dS' = \sum_{i=1}^{3} F_{s\,(i)} \tag{A6a}$$

$$F_{s\,(i)} = |d_{(i)}| \left(\arctan\left[\frac{N_{1\,(i)}}{D_{1\,(i)}}\right] - \arctan\left[\frac{N_{2\,(i)}}{D_{2\,(i)}}\right] \right) + \ln\left[\frac{S_{2\,(i)}}{S_{1\,(i)}}\right] P_{o\,(i)} \tag{A6b}$$

$$D_{1\,(i)} = R^2_{o\,(i)} + |d_{(i)}| R_{1\,(i)} \tag{A6c}$$

$$D_{2\,(i)} = R^2_{o\,(i)} + |d_{(i)}| R_{2\,(i)} \tag{A6d}$$

$$N_{1\,(i)} = P_{o\,(i)} l_{1\,(i)} \tag{A6e}$$

$$N_{2\,(i)} = P_{o\,(i)} l_{2\,(i)} \tag{A6f}$$

$$S_{1\,(i)} = R_{1\,(i)} + l_{1\,(i)} \tag{A6g}$$

$$S_{2\,(i)} = R_{2\,(i)} + l_{2\,(i)} \tag{A6h}$$

Finally, we have:

$$\mathbf{I}_1(\mathbf{r}) = \nabla I_{aux,1} = \sum_{i=1}^{3} \nabla F_{s\,(i)} \tag{A7a}$$

$$\nabla F_{s\,(i)} = \frac{\partial F_{s\,(i)}}{\partial x}\hat{\mathbf{x}} + \frac{\partial F_{s\,(i)}}{\partial y}\hat{\mathbf{y}} + \frac{\partial F_{s\,(i)}}{\partial z}\hat{\mathbf{z}} \tag{A7b}$$

where the partial derivatives can be obtained as:

$$F'_{s\,(i)} = \left(\arctan\left[\frac{N_{1\,(i)}}{D_{1\,(i)}}\right] - \arctan\left[\frac{N_{2\,(i)}}{D_{2\,(i)}}\right]\right)\operatorname{sign}[d_{(i)}]d'_{(i)}$$
$$+ |d_{(i)}|\left(\frac{-N_{1\,(i)}D'_{1\,(i)} + D_{1\,(i)}N'_{1\,(i)}}{D^2_{1\,(i)} + N^2_{1\,(i)}} - \frac{-N_{2\,(i)}D'_{2\,(i)} + D_{2\,(i)}N'_{2\,(i)}}{D^2_{2\,(i)} + N^2_{2\,(i)}}\right) \tag{A8}$$
$$+ \ln\left[\frac{S_{2\,(i)}}{S_{1\,(i)}}\right]P'_{o\,(i)} + P_{o\,(i)}\left(-\frac{S'_{1\,(i)}}{S_{1\,(i)}} + \frac{S'_{2\,(i)}}{S_{2\,(i)}}\right)$$

In this equation, $f' = \partial f/\partial\eta$, with $\eta = x, y, z$ representing the classical rectangular coordinates.

A2. Calculation of $\mathbf{I}_{E_2}^{(sing)}(\mathbf{r})$

The evaluation of this singular integral has been already discussed in [*Arcioni et al.*, 1997]. Following the guidelines that can be found in such contribution, a closed form expression can be derived:

$$\mathbf{I}_2(\mathbf{r}) = \int_{S'}\frac{1}{R}\left(\bar{\mathbf{I}} + \frac{\mathbf{RR}}{R^2}\right)\cdot\mathbf{f}_n(\mathbf{r}')\,dS' = 4\mathbf{I}_W(\mathbf{r}) + 2(\mathbf{r} - \mathbf{r}_\beta - 2d\hat{\mathbf{n}})I_{aux,1} + \mathbf{I}_{NC}(\mathbf{r}) \tag{A9}$$

where we have defined:

$$\mathbf{I}_W(\mathbf{r}) = \frac{1}{2}\hat{\mathbf{u}}\sum_{i=1}^{3}\ln\left[\frac{S_{2\,(i)}}{S_{1\,(i)}}\right]R^2_{o\,(i)} + B_{(i)} \tag{A10a}$$

$$B_{(i)} = \frac{1}{2}P_{o\,(i)}(R_{2\,(i)}l_{2\,(i)} - R_{1\,(i)}l_{1\,(i)}) \tag{A10b}$$

$$\mathbf{I}_{NC}(\mathbf{r}) = (\mathbf{R}_1 - \mathbf{t}_\beta\mathbf{R}_1\cdot\mathbf{t}_\beta)h_\beta\ln\frac{|\mathbf{R}_1| + \mathbf{t}_\beta\cdot\mathbf{R}_1}{|\mathbf{R}_2| + \mathbf{t}_\beta\cdot\mathbf{R}_2} - \mathbf{t}_\beta h_\beta(|\mathbf{R}_2| - |\mathbf{R}_1|) \tag{A10c}$$

$$\mathbf{t}_\beta = \frac{\mathbf{R}_2 - \mathbf{R}_1}{|\mathbf{R}_2 - \mathbf{R}_1|} \tag{A10d}$$

being $\mathbf{R}_1$ and $\mathbf{R}_2$ vectors defined with respect to the line segment opposite to the vertex pointed by vector $\mathbf{r}_\beta$ (see Fig. 1 for more details on the different scalar and vector variables).

A3. Calculation of $\mathbf{I}_{H_1}^{(sing)}(\mathbf{r})$

The singular term $\mathbf{I}_{H_1}^{(sing)}(\mathbf{r})$ can be computed starting from (A9). In fact:

$$\mathbf{I}_3(\mathbf{r}) = \int_{S'} \nabla \times \frac{1}{R}\left(\bar{\mathbf{I}} + \frac{\mathbf{RR}}{R^2}\right) \cdot \mathbf{f}_n(\mathbf{r}')\, dS' = \nabla \times \mathbf{I}_2(\mathbf{r}) \qquad \text{(A11)}$$

Therefore, we can readily derive:

$$\mathbf{I}_3(\mathbf{r}) = 4\nabla \times \mathbf{I}_W(\mathbf{r}) + 2\nabla I_{aux,1} \times (\mathbf{r} - \mathbf{r}_\beta - 2d\hat{\mathbf{n}}) \qquad \text{(A12)}$$

since $\nabla \times \mathbf{I}_{NC}(\mathbf{r}) = 0$. Besides, it is important to point out that the calculation of $\nabla I_{aux,1}$ has been already performed in (A7a). Finally, the curl of the vector function $\mathbf{I}_W(\mathbf{r})$ can be easily obtained starting from the next partial derivatives:

$$\mathbf{I}'_W = \frac{1}{2}\hat{\mathbf{u}} \sum_{i=1}^{3} \ln\left[\frac{S_{2\,(i)}}{S_{1\,(i)}}\right] 2R_{o\,(i)}R'_{o\,(i)} + R^2_{o\,(i)}\left(-\frac{S'_{1\,(i)}}{S_{1\,(i)}} + \frac{S'_{2\,(i)}}{S_{2\,(i)}}\right) + B'_{(i)} \qquad \text{(A13a)}$$

$$B'_{(i)} = \frac{1}{2}P'_{o\,(i)}(R_{2\,(i)}l_{2\,(i)} - R_{1\,(i)}l_{1\,(i)}) + \frac{1}{2}P_{o\,(i)}(R'_{2\,(i)}l_{2\,(i)} + R_{2\,(i)}l'_{2\,(i)} - R'_{1\,(i)}l_{1\,(i)} - R_{1\,(i)}l'_{1\,(i)}) \qquad \text{(A13b)}$$

If the observation point is exactly located on the line segment of a triangular cell acting as a source point, it is possible to demonstrate that the field cannot be longer calculated using (A7a). Even in this case, an accurate computation of the electric and magnetic fields can be performed making use of the continuity equation. We can obtain:

$$\mathbf{E}(\mathbf{r}) = -\,\hat{\mathbf{n}} \cdot \frac{\sum_{n=1}^{N_{cs}} d_n^{cs} \nabla \cdot \mathbf{f}_{ns}(\mathbf{r})}{j\omega\epsilon_r\epsilon_0} \qquad \text{(A14a)}$$

$$\mathbf{H}(\mathbf{r}) = -\,\mathbf{J}_s \times \hat{\mathbf{n}} = -\left(\sum_{n=1}^{N_{cs}} d_n^{cs}\, \mathbf{f}_{ns}(\mathbf{r})\right) \times \hat{\mathbf{n}} \qquad \text{(A14b)}$$

being N_{cs} the number of RWG basis functions $\mathbf{f}_{ns}(\mathbf{r})$ defined on the triangular cell acting as a source point, and d_n^{cs} the expansion coefficients defined in (11). It is very important to note that the expresions (A14) provide a very simple formulation for computing the electromagnetic field on the source points, not only avoiding the numerical instabilities present in (12), but also significantly reducing the computational effort related to this calculation.

Acknowledgments. All the data necessary to understand, evaluate, replicate, and generate the figures and results presented in this paper have been included in the present manuscript. The commercial software FEST3D has been used to generate the simulated results provided by the authors.

This work was supported by the Ministerio de Economía y Competitividad, Spanish Government, under the Research Projects TEC2013-47037-C5-1-R and TEC2013-47037-C5-4-R.

References

Arcioni, P., M. Bozzi, M. Bressan, G. Conciauro, and L. Perregrini (2002), Frequency/time-domain modeling of 3D waveguide structures by a BI-RME approach, *Int. J. Numer. Model.-Electron. Netw. Device Fields*, *15*(1), 3–21.

Arcioni, P., M. Bressan, and L. Perregrini (1997), On the evaluation of the double surface integrals arising in the application of the boundary integral method to 3-D problems, *IEEE Trans. Microw. Theory Tech.*, *45*(3), 436–439.

Bressan, M., and G. Conciauro (1985), Singularity extraction from the electric Green's function for a spherical resonator, *IEEE Trans. Microw. Theory Tech.*, *33*(5), 407–414.

Cameron, R., C. Kudsia, and R. Mansour (2007), *Microwave Filters for Communication Systems: Fundamentals, Design and Applications*, Wiley, Chichester.

Cogollos, S., V. E. Boria, P. Soto, B. Gimeno, and M. Guglielmi (2001), Efficient CAD tool for inductively coupled rectangular waveguide filters with rounded corners, *Proc. 31st Eur. Microw. Conf.*, 1–4.

Conciauro, G., M. Guglielmi, and R. Sorrentino (2000), *Advanced Modal Analysis - CAD Techniques for Waveguides Components and Filters*, Wiley, Chichester.

Cools, R. (1999), Monomial cubature rules since Stroud: A compilation, part. 2, *J. Comput. Appl. Math.*, *112*, 21–27.

El Sabbagh, M., K. A. Zaki, H. Yao, and M. Yu (2001), Full-Wave analysis of coupling between combline resonators and its application to combline filters with canonical configurations, *IEEE Trans. Microw. Theory Tech.*, *49*(12), 2384–2393.

Gerini, G., and M. Guglielmi (2001), Full-wave CAD of a rectangular waveguide filter with integrated coaxial excitation, *IEEE Trans. Microw. Theory Tech.*, *49*(5), 986–990.

Golub, G. H., and C. F. Van Loan (1996), *Matrix Computations*, John Hopkins University Press, Baltimore.

Mira, F., A. A. San Blas, V. E. Boria, L. J. Roglà, and B. Gimeno (2013), Wideband generalized admittance matrix representation for the analysis and design of waveguide filters with coaxial excitation, *Radio Sci.*, *48*, 1–11.

Mira, F., M. Bressan, G. Conciauro, B. Gimeno, and V. E. Boria (2005), Fast S-domain method of rectangular waveguides with radially-symmetric metal insets, *IEEE Trans. Microw. Theory Tech.*, *53*(4), 1294–1303.

Quesada, F. D., A. Vidal, F. J. Pérez, A. Berenguer, A. A. San Blas, F. Mira, V. E. Boria, B. Gimeno, and A. Álvarez (2010), Broad band analysis of arbitrarily shaped microwave filters using a novel singular value decomposition technique, *Proc. 4th Eur. Conf. on Ant. and Prop.*, 1–2.

Rao, S. M., D. R. Wilton, and A. W. Glisson (1982), Electromagnetic scattering by surfaces of arbitrarily shape, *IEEE Trans. Antennas Propagat.*, *30*(5), 409–418.

Ruiz-Cruz, J. A., K. A. Zaki, J. R. Montejo-Garai, and J. Rebollar (2005), Rectangular waveguide elliptic filters with capacitive and inductive irises and integrated coaxial excitation, *IEEE MTT-S Int. Microw. Symp. Dig.*, 269–272.

Uher, J., J. Bornemann, and U. Rosenberg (1993), *Waveguide Components for Antenna Feed Systems: Theory and CAD*, Artech House, Norwood.

Wang, C., K. A. Zaki, A. E. Atia, and T. G. Dolan (1998), Dielectric combline resonators and filters, *IEEE Trans. Microw. Theory Tech.*, *46*(12), 2501–2506.

Wilton, D. R., S. M. Rao, A. W. Glisson, D. H. Schaubert, O. M. Al-Bundak, and C. M. Butler (1984), Potential integrals for uniform and linear source distributions on polygonal and polyhedral domains, *IEEE Trans. Antennas Propagat.*, *32*, 276–281.

Yao, H., K. A. Zaki, A. E. Atia, and R. Hershtig (1995), Full-wave modeling of conducting posts in rectangular waveguides and its applications to slot coupled combline filters, *IEEE Trans. Microw. Theory Tech.*, *43*(12), 2824–2830.

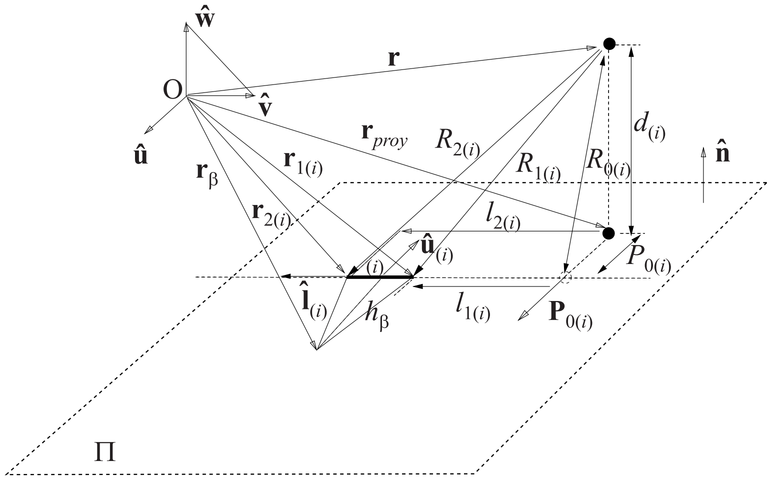

Figure 1. Geometrical quantities associated with the line segment (i) lying in the plane Π.

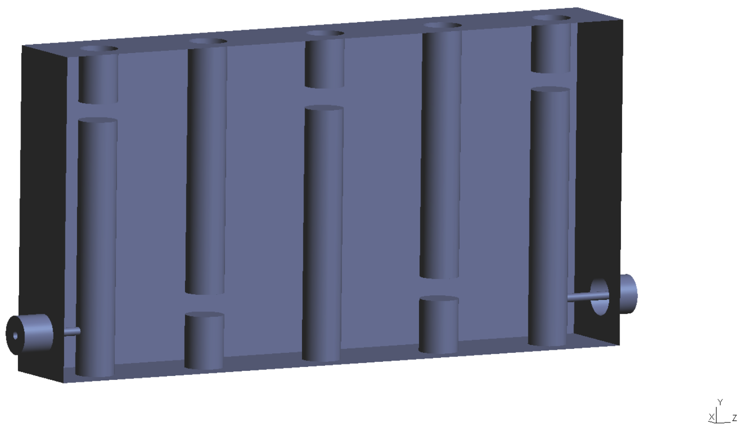

Figure 2. Interdigital band-pass filter composed of 5 resonators. The coaxial probe is in contact with the metallic posts of the input and output resonators.

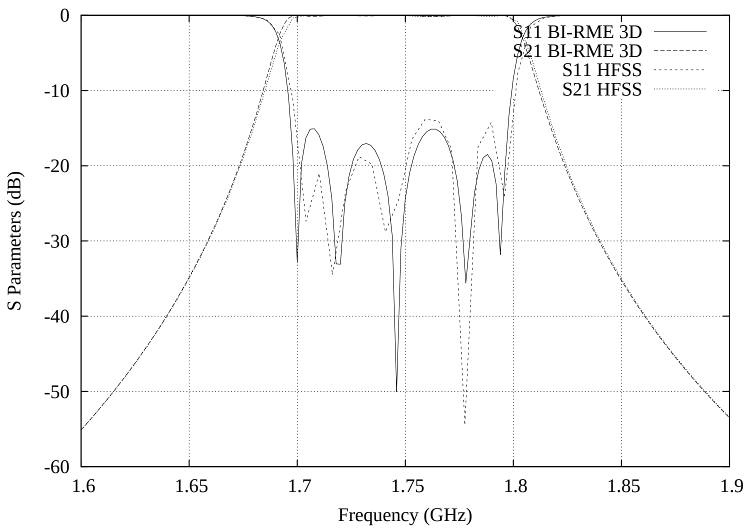

Figure 3. S-parameters of the interdigital filter of Fig. 2.

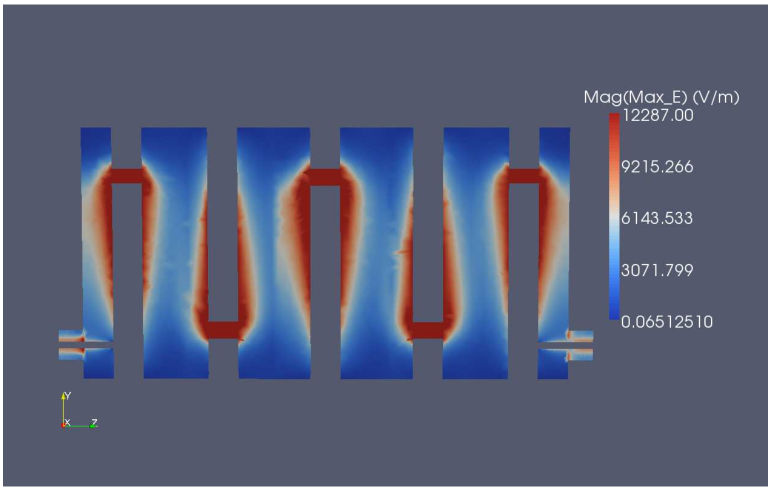

a)

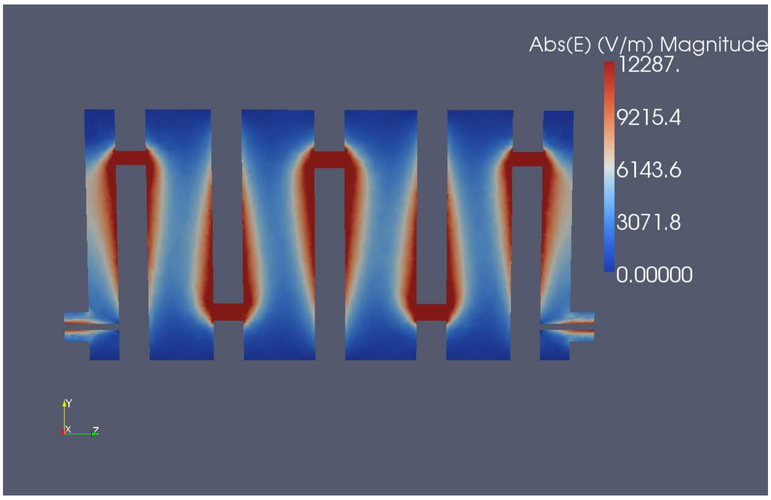

b)

Figure 4. Magnitude (V/m) of the electric field of the interdigital filter computed at $f = 1.75$ GHz on the $x = 0$ plane. a) 3D BI-RME simulated results. b) HFSS simulated data.

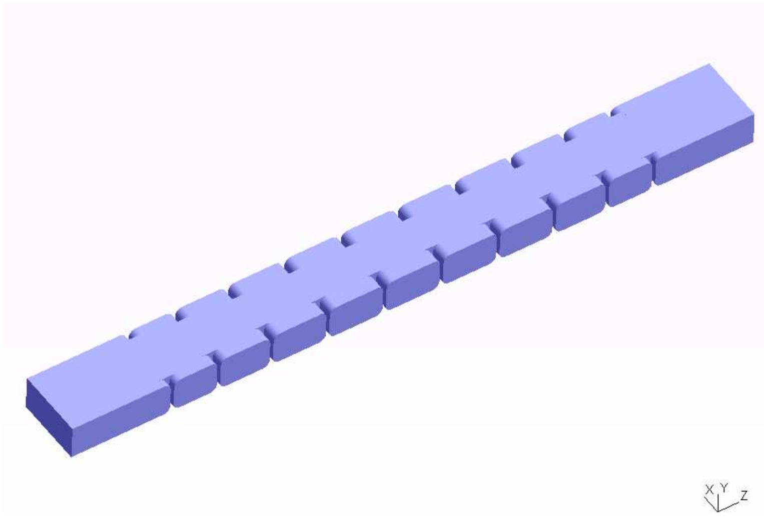

Figure 5. Inductive iris waveguide filter with rounded corners.

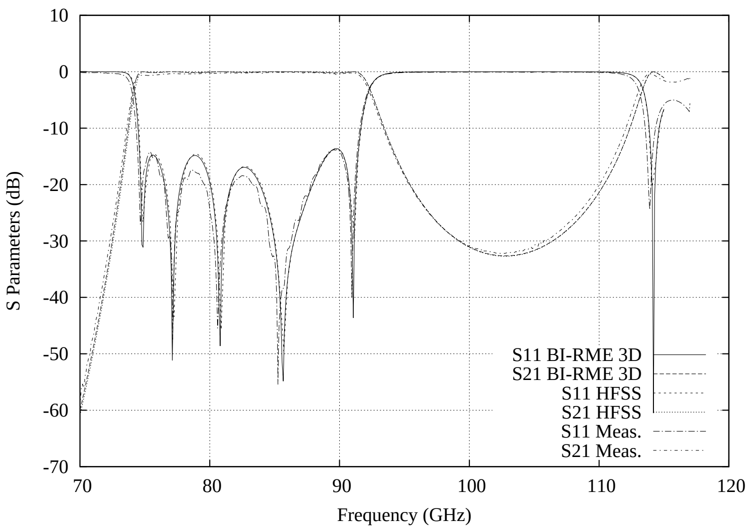

Figure 6. S-parameters of the manufactured inductive filter represented in Fig. 5.

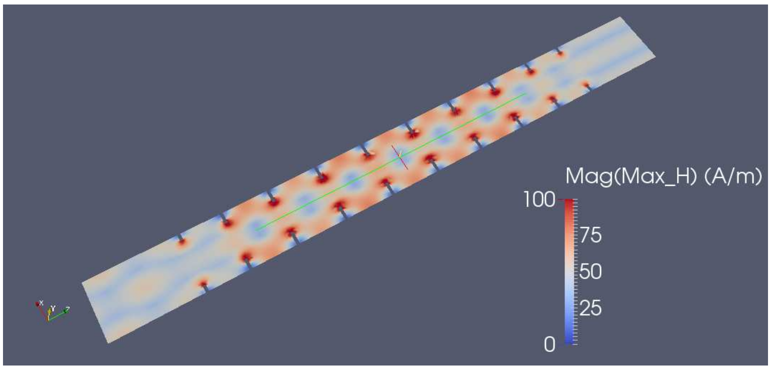

a)

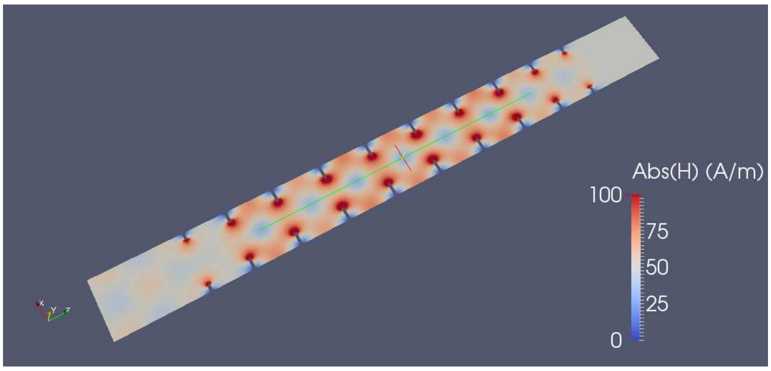

b)

Figure 7. Magnitude (A/m) of the magnetic field of the inductive iris waveguide filter at $f = 83$ GHz on the $y = 0$ plane. a) 3D BI-RME simulated results. b) HFSS simulated data.

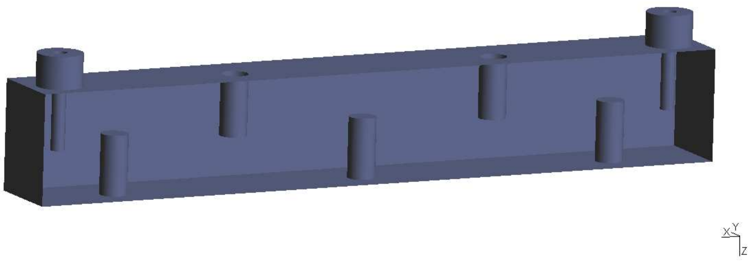

Figure 8. X-band evanescent-mode filter. A top coaxial feed configuration is used in this design.

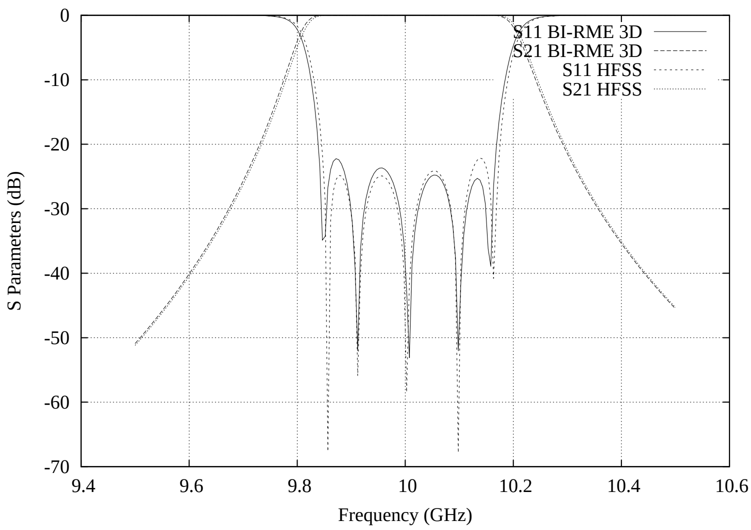

Figure 9. S-parameters of the evanescent-mode filter designed in Fig. 8.

Table 1. Dimensions of the resonators of the interdigital filter of Fig. 2 (all data in mm).

Resonator	Length	Height of post	Height of screw
1, 5	19.262	39.027	8.144
2	17.0	38.536	8.067
3	21.217	38.545	8.109
4	17.0	38.536	8.088

Table 2. Length of the uniform waveguide sections used between the resonators of the interdigital filter of Fig. 2 (all data in mm).

Waveguide section	Length
1, 4	0.207
2, 3	1.287

Table 3. Widths of the inductive irises of the filter of Fig. 5 (all data in mm).

Iris	Width
1, 10	1.966
2, 9	1.638
3, 8	1.435
4, 7	1.399
5, 6	1.384

Table 4. Lengths of the resonators of the inductive filter of Fig. 5 (all data in mm).

Resonator	Length
1	1.106
2, 8	1.342
3	1.464
4, 6	1.487
5	1.492
7	1.463
9	1.108

Table 5. Dimensions of the rectangular cavities of the evanescent-mode filter of Fig. 8 (all data in mm).

Cavity	Length	Height of post
2, 6	4.5	5.508
3, 4, 5	6.0	5.542

Table 6. Length of the uniform waveguide sections used between the cavities of the evanescent-mode filter of Fig. 8 (all data in mm).

Waveguide section	Length
1, 6	0.367
2, 5	6.45
3, 4	6.78